inotiv
analyze. answer. advance.

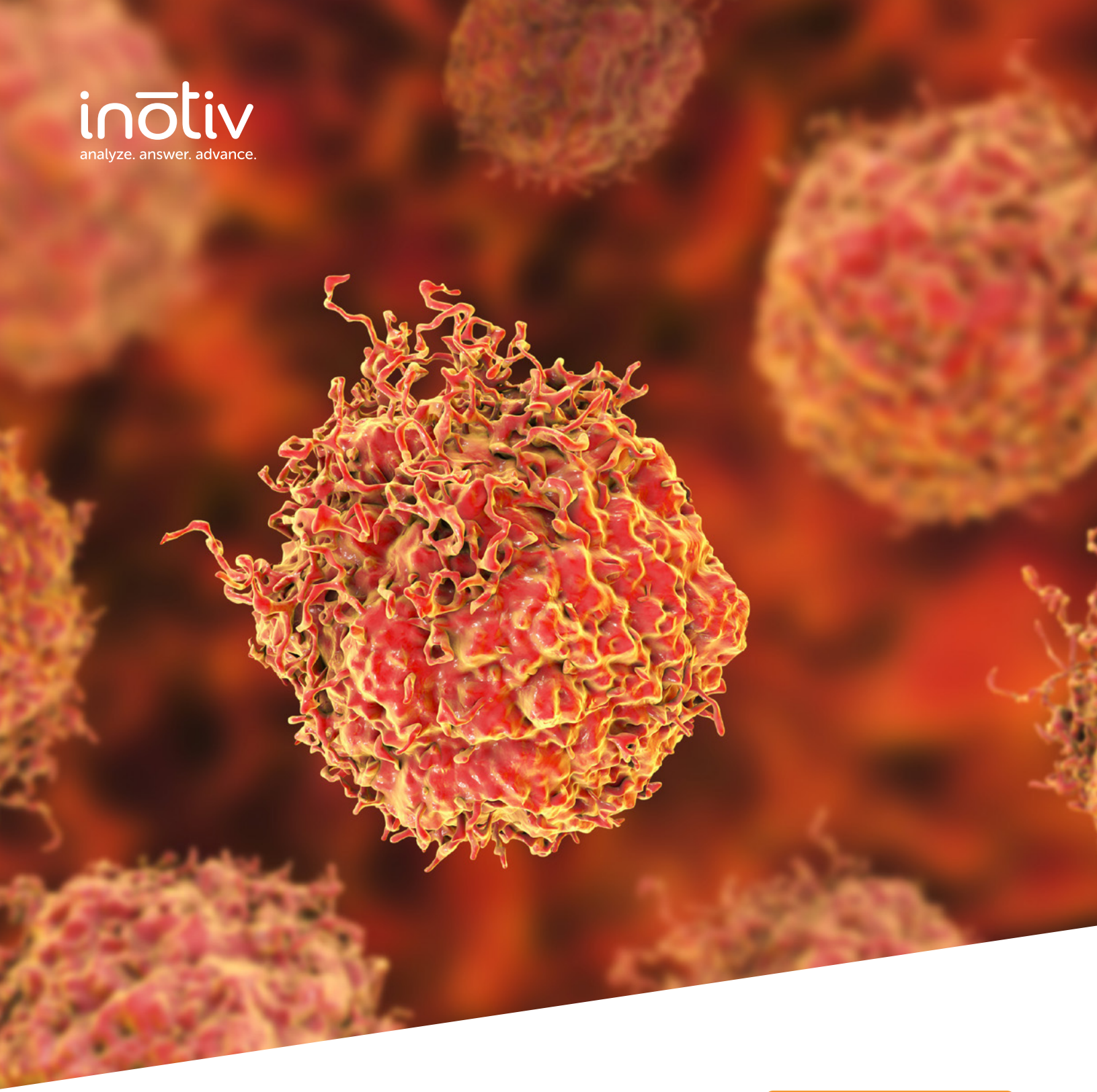

White Paper // July 2020

Characterization, Development, and Applications

OF THE NOVEL ULTRA-IMMUNODEFICIENT B-NDG MOUSE

Immunodeficient mice are important tools in advancing basic research and drug discovery and development activities. They are being **used in an increasing number of research fields**, including oncology, immunology, immuno-oncology, precision medicine, and stem cell biology.

The B-NDG (NOD.CB17-*Prkdc*^{scid} *IL2rg*^{tm1}/BcgenHsd) knockout mouse is a highly immunodeficient model that is a new alternative option among this category of models. This mouse was developed by Biocytogen and is now commercially available from Inotiv. Envigo licensed the model from Biocytogen in 2019, then Envigo was acquired by Inotiv in 2021. B-NDG is an albino single-gene knockout mouse that was generated by deleting the common gamma chain (*IL2rg*) gene in NOD-scid mice using CRISPR-Cas9 technology (Figure 1).

Figure 1: CRISPR-Cas9 technology was used to delete the *IL2rg* gene in NOD-scid mice.

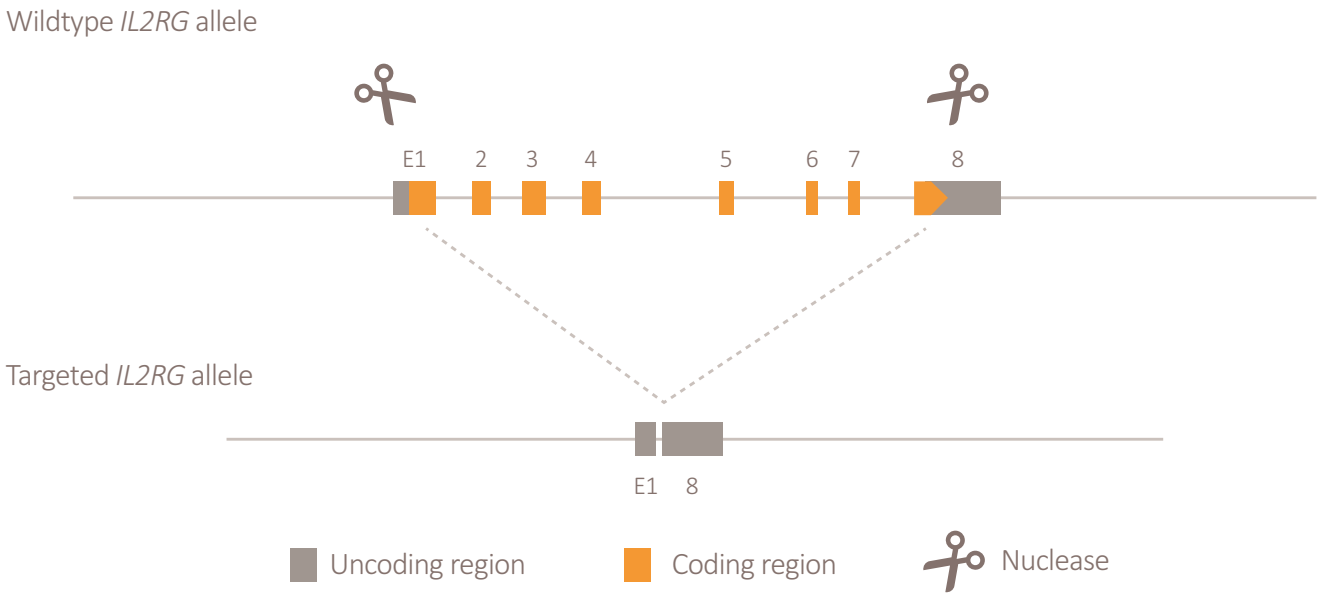

The B-NDG mouse builds upon the well-known immunodeficiencies associated with NOD-scid mice, including significant deficiencies in functional T and B cells, due to the spontaneous loss-of-function mutation in the *Prkdc* (protein kinase, DNA-activated, catalytic subunit) gene.

IN COMPARISON, THE B-NDG MOUSE:

- lacks mature T and B cells,
- lacks functional natural killer (NK) cells, and
- displays a deficiency in cytokine signaling.

These features make the B-NDG mouse one of the most highly immunodeficient models available on the market. It is suitable for engraftment with human cancer cells or tissue, including for developing patient-derived xenograft (PDX) tumor models and humanized models with CD34+ human hematopoietic stem cells (HSCs) or peripheral blood mononuclear cells (PBMCs). The B-NDG mouse has served successfully in dozens of peer-reviewed publications for a variety of applications (see references). More than 300 PDX models have been successfully established across many tumor types, including breast, colon, gastric, lung, pancreatic, and several blood tumors (AML and ALL) (Table 1; Lin 2019).

Table 1: PDX models established using the B-NDG mouse and their respective success rates for establishing the models.

TUMOR	TOTAL SAMPLES	FAILED	UNDER OBSERVATION	SUCCESSFUL	SUCCESS RATE
Blood	111	52	25	34	40%
Breast	255	204	35	16	7%
Gastric	546	305	50	191	39%
Lung	193	143	1	48	25%
Colorectal	63	15	33	15	50%
Esophagus	39	18	0	21	26%
Pancreatic	89	60	8	21	26%
TOTAL	1,296	797	152	346	35%

Successful rate = Successful / (Successful + Failed); excludes the samples still under observation

The remainder of this white paper provides a characterization of the B-NDG mouse, including its growth curve and immune cell phenotyping, and examples of various models that have been developed using it, including a cell line-derived xenograft (CDX), PDX, and humanized models.

Characteristics of the B-NDG mouse

GROWTH CHART

A cohort of B-NDG mice (N = 50 males and 50 females) were weighed the same day each week from 3 to 9 weeks of age. The average body weight (in grams) of the male (Orange) and female (Grey) mice was plotted over the course of the study, and the results are shown in Figure 2. Beginning at approximately week 4, the males begin to have a higher average weight.

Figure 2: Growth curve for male and female B-NDG mice from 3 to 9 weeks of age.

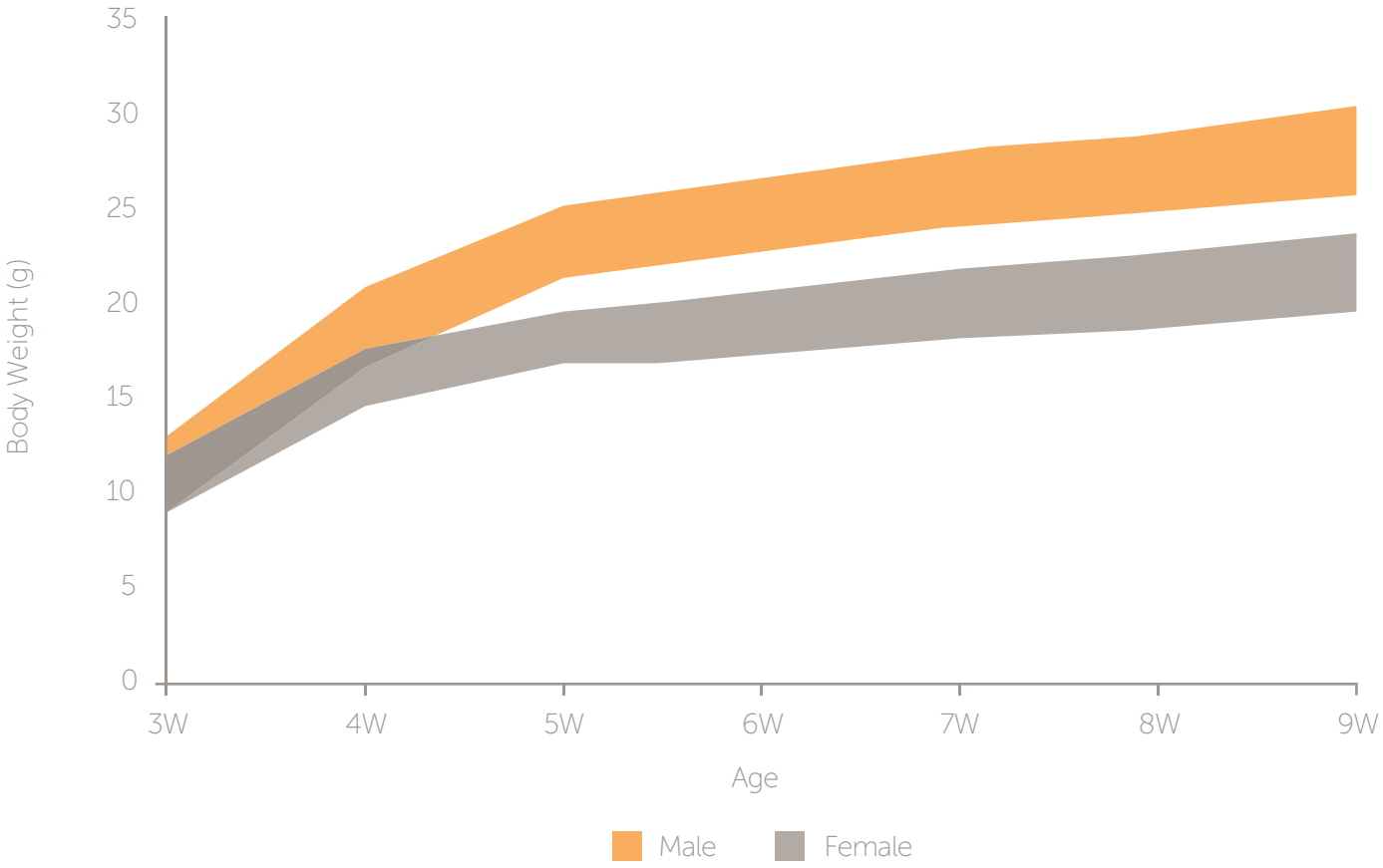

COMPLETE BLOOD COUNT

The following plots show the complete blood count results for B-NDG mice (dark grey bars) compared to control C57BL/6 mice (green bars) (Figure 3A and 3B). B-NDG animals show greatly reduced white blood cell (WBC) and lymphocyte (LY#) counts (Figure 3A) and an increase in platelets (Figure 3B). No other significant changes were detected in the blood count parameters that were evaluated.

Figure 3: Complete blood count for B-NDG and control C57BL/6 mice.

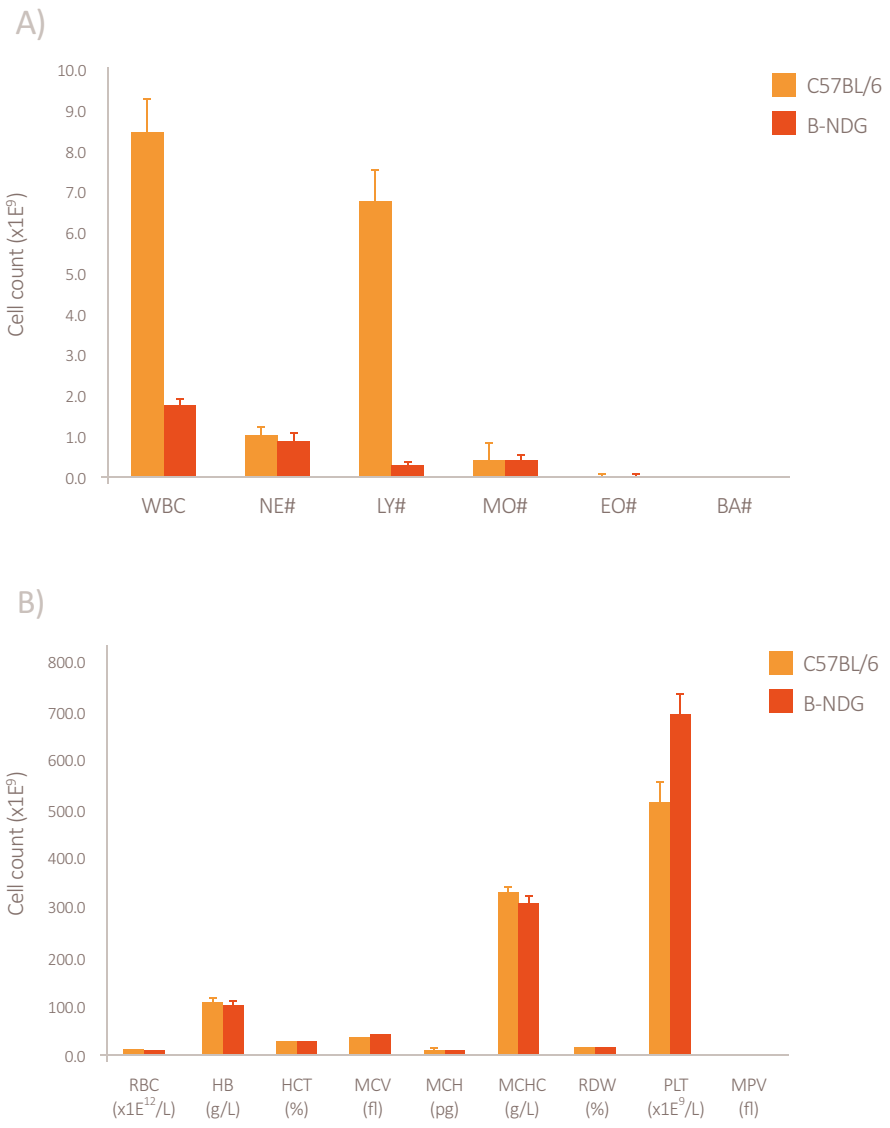

*Abbreviations: WBC = white blood cell; NE# = neutrophil count; LY# = lymphocyte count; MO# = monocyte count; EO# = eosinophil count; BA# = basophil count; RBC = red blood cell; HB = hemoglobin; HCT = hematocrit; MCV = mean corpuscle (cell) volume; MCH = mean corpuscular hemoglobin; MCHC = mean corpuscular hemoglobin concentration; RDW = red cell distribution width; PLT = platelet count; MPV = mean platelet volume.

FLOW CYTOMETRY IMMUNOPHENOTYPING

Splenocytes of control C57BL/6, NOD-scid, and B-NDG mice were isolated and examined via flow cytometry for total B cells (CD19+/TCRβ+), NK cells (NKp46+), CD4+ T cells (CD4+), CD8+ T cells (CD8+/CD4+), and regulatory T cells (Foxp3+/CD4+) (Figure 4A). IL2rg gene deletion results in a lack of functional receptors for IL-2, IL-4, IL-7, IL-9, IL-15, and IL-21, which leads to cytokine signaling deficiencies and the lack of functional NK cells. Figure 4B shows that NKp46 expression was detected in splenocytes and blood cells of C57BL/6 but not B-NDG mice, indicating the absence of NK cells.

Figure 4: (A) Flow cytometry data of splenocytes from C57BL6, NOD-scid and B-NDG mice. Data shows a complete lack of T, B, and NK cells in the B-NDG model. (B) NKp46 expression in splenocytes and blood cells.

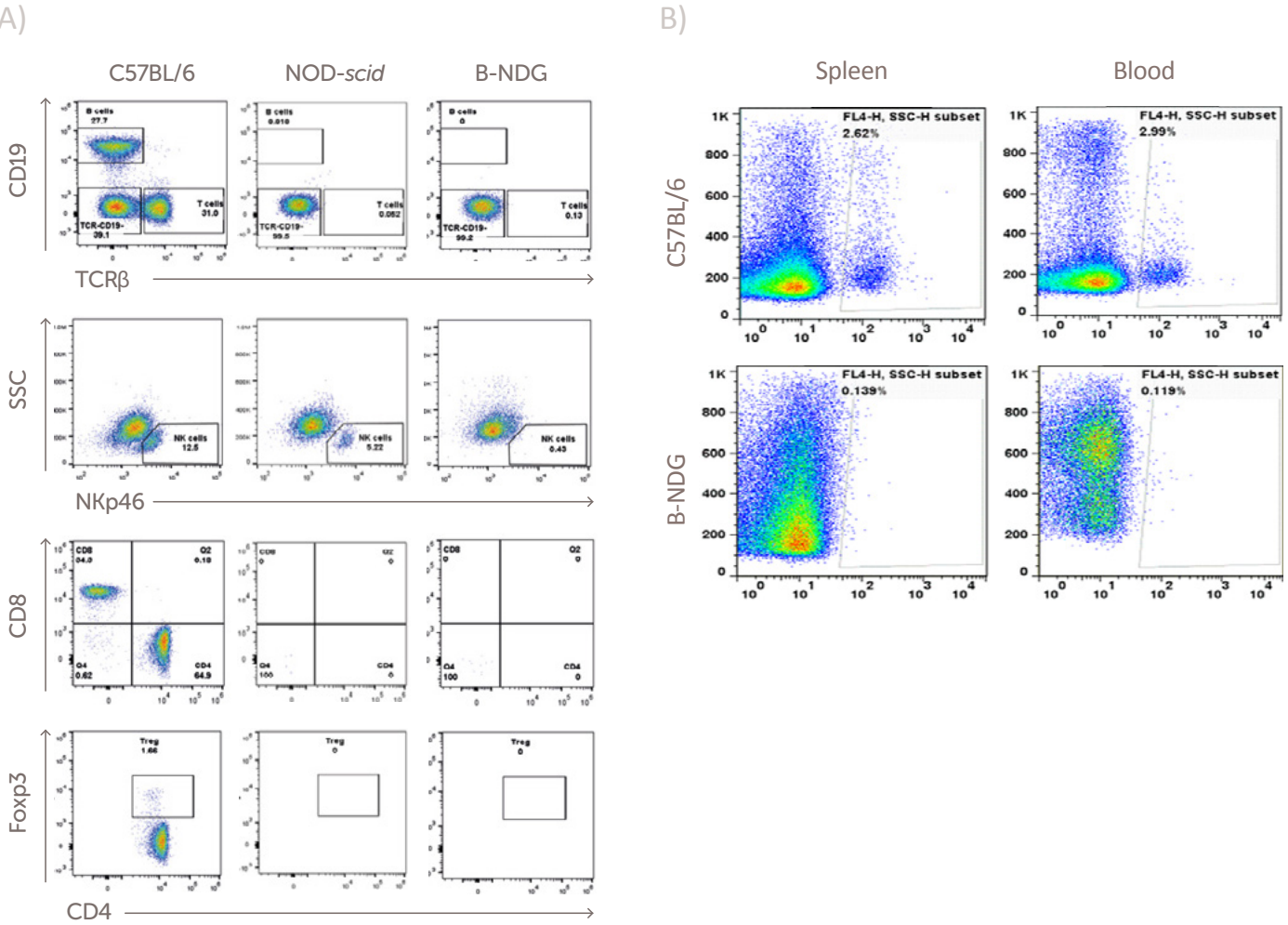

Disease models using the B-NDG Mouse

Development of a Humanized Immune System Model

This section describes two methods for humanizing B-NDG mice: (1) human PBMCs (hPBMCs), and (2) HSCs.

FIRST METHOD: HUMANIZED MODEL USING hPBMCs

B-NDG mice (n = 3) were injected with 5x10^6 hPBMCs into their caudal veins. The percentage and type of mouse and human CD45+ (mCD45+ and hCD45+, respectively) cells were determined via flow cytometry 24 days post injection.

As shown in Figure 5 (top panel), the three mice had between 36–73% hCD45+ cells, of which over 99% were identified as T cells (CD19+/CD3+) in all three animals (Figure 5, bottom panel).

Figure 5: Humanization of B-NDG mice with hPBMCs at 24 days post injection.

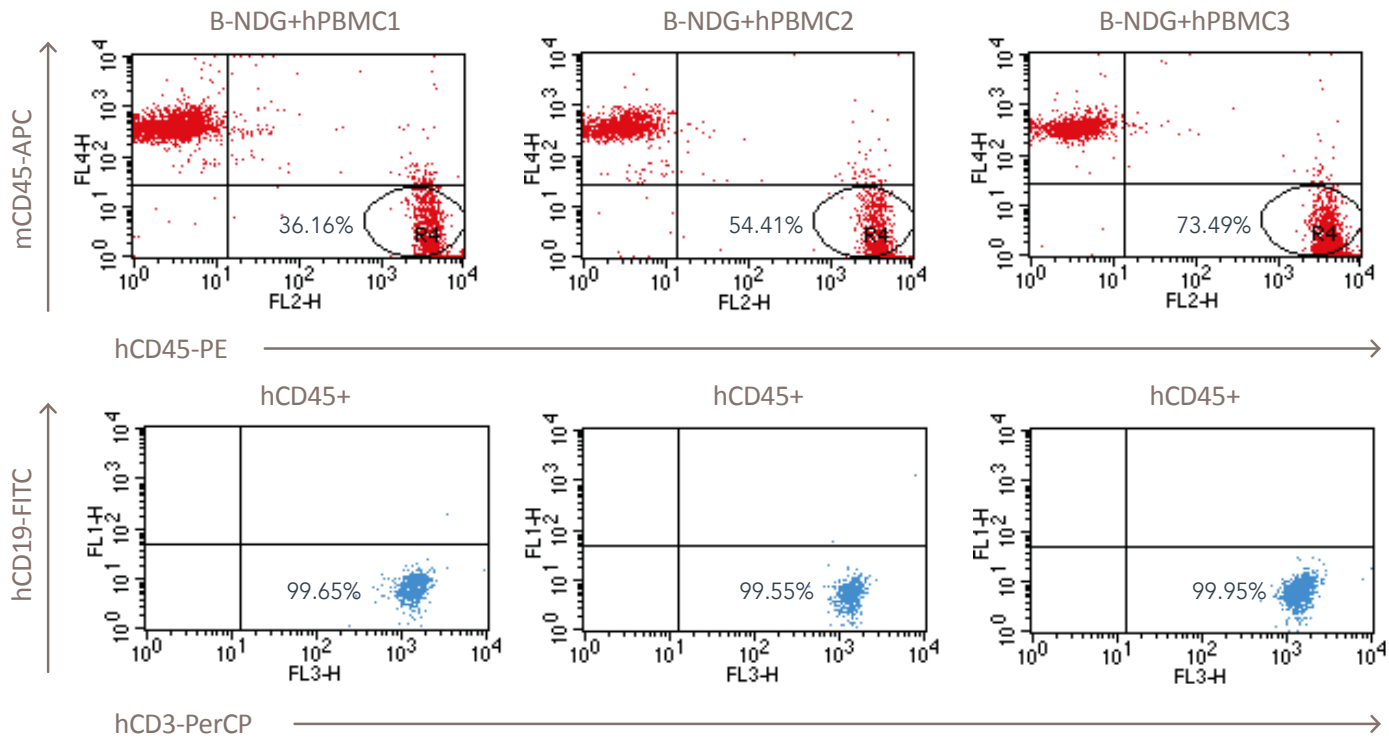

SECOND METHOD: HUMANIZED MODEL USING HSCs

B-NDG mice were injected intravenously with human CD34+ HSCs (after irradiation) using either $1x10^5$ or $2x10^5$ cells. After injection with $1x10^5$ human CD34+ HSCs, the percentage of human CD45+ cells in the peripheral blood was determined using flow cytometry. As shown in Figure 6A, over 70% of engrafted animals had more than 80% of these cells by eight weeks post injection.

At 16 weeks post injection, the percentages of the total number of human lymphocytes in the humanized mice were 49% for T cells, 25.2% for B cells, and 2.2% for NK cells (Figure 6B), suggesting that human T, B, and NK cells in reconstituted B-NDG mice were successfully propagated. There were no human cells present in the control group (no injection of CD34+ cells; data not shown). Notably, the percentage of human T cells increased steadily over the extended observation window.

Figure 6: Humanization of B-NDG mice with CD34+ HSCs (A) Percentage of human CD45+ cells in the peripheral blood over eight weeks. (B) Percentages of total human lymphocytes (T, B, and NK cells) at 16 weeks post injection.

Figure 6A:

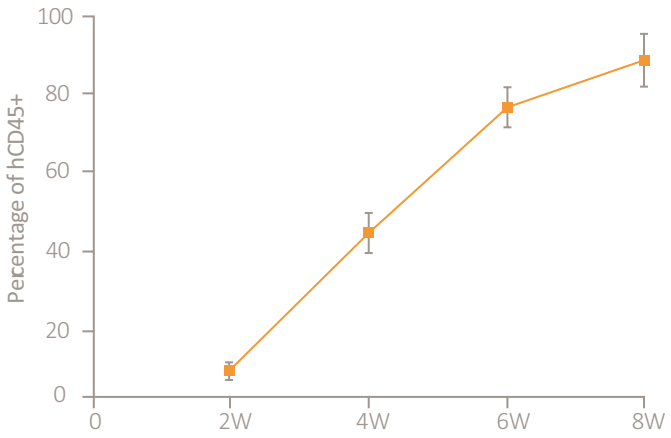

Figure 6B:

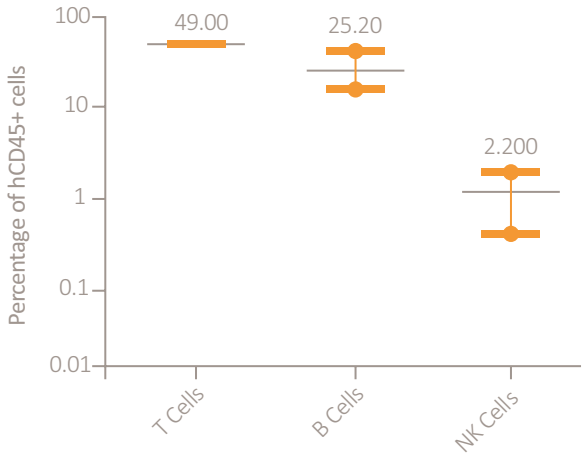

After injection of B-NDG mice with $2x10^5$ CD34+ cells, flow cytometric analysis of peripheral blood was conducted at 10 weeks post engraftment (Figure 7). As compared to the control animals (BALB/c and B-NDG mice without injection of CD34+ cells) that showed a lack of human cells, the humanized B-NDG mice had high percentages of human CD45+ cells (Figure 7, first column of panels) and multilineage cells, including CD3+ T cells (Figure 7, bottom row of panels).

Figure 7: Humanization of B-NDG mice with CD34+ HSCs.

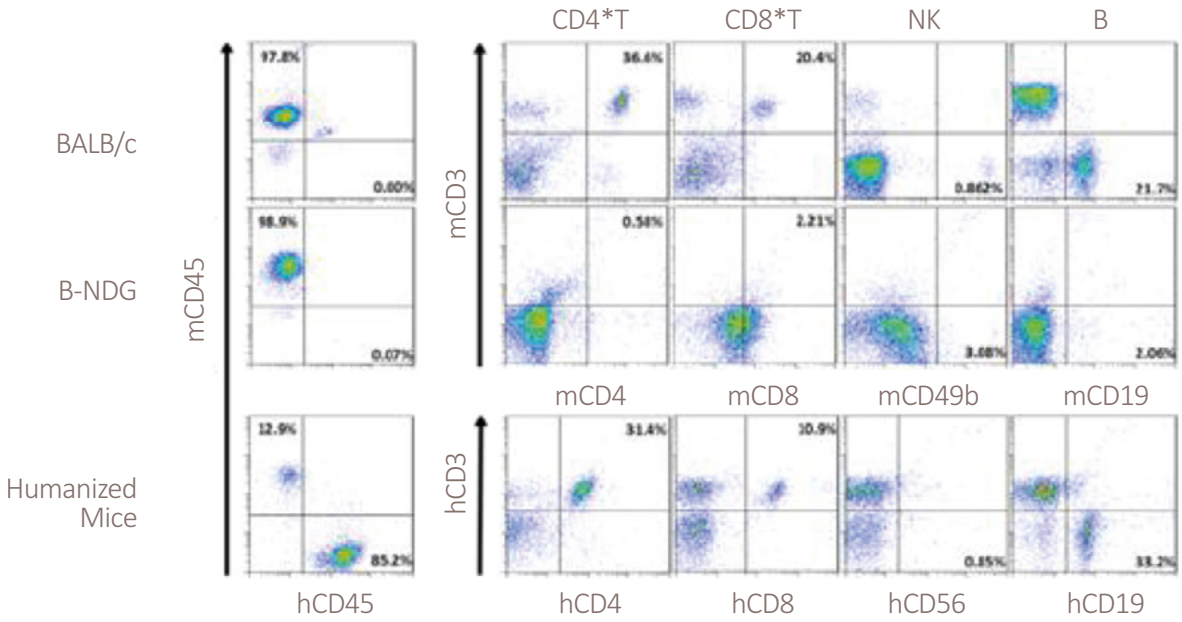

The survival of humanized B-NDG mice (using CD34+ HSCs) was also evaluated. After irradiation and cell engraftment (n = 5), the survival rate was significantly higher via reconstitution with human CD34+ cells when compared to control animals that were irradiated but not engrafted with CD34+ cells (Figure 8).

Figure 8: Survival of B-NDG mice after irradiation and injection of human CD34+ cells.

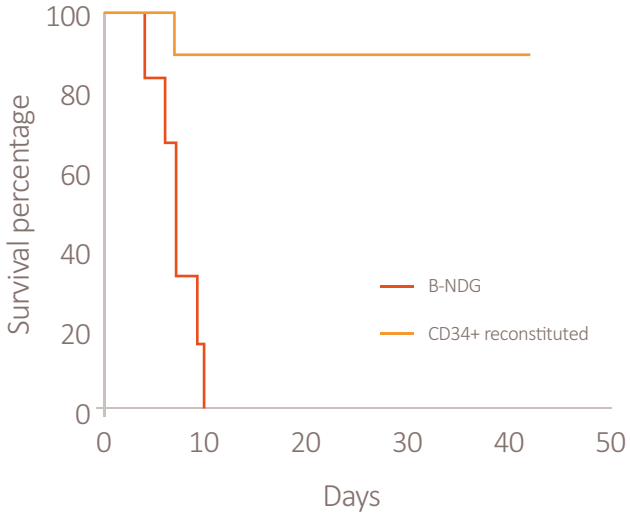

Development of a Gastric Cancer PDX Model

A gastric cancer PDX model was developed in B-NDG and C.B17 scid mice (n = 6), and tumor size was measured using calipers through day 60 post implantation. In contrast to C.B17 scid mice, which had a tumor take rate of 0% (Figure 9A), the rate in B-NDG was 66.7% (4/6) (Figure 9A). Figure 9A also shows the time for tumors to reach 250 mm^3 in size for the four PDXs that were successfully established. The average tumor growth rate to 2000 mm^3 over the 60 days is shown in Figure 9B for B-NDG mice, with an average tumor doubling time of 6.75 days.

Figure 9: Gastric cancer PDX growth in C.B17 *scid* and B-NDG mice. (A) Take rate in B-NDG mice and C.B17 *scid* mice, the doubling time for each mouse, and the time to grow to 250 mm^3. (B) Average tumor growth in B-NDG mice by day 60 post implantation.

GASTRIC CANCER PDX	CB17-*scid*	B-NDG	
ID	Tumor size to 250mm^3	Tumor Size to 250mm^3	Tumor doubling time
1	-	40 days	7 days
2	-	56 days	5 days
3	-	66 days	10 days
4	-	-	-
5	-	-	-
6	-	40 days	5 days
	Tumor take rate 0% (0/6)	Tumor take rate 66.7% (4/6)	Average doubling time 6.75 days

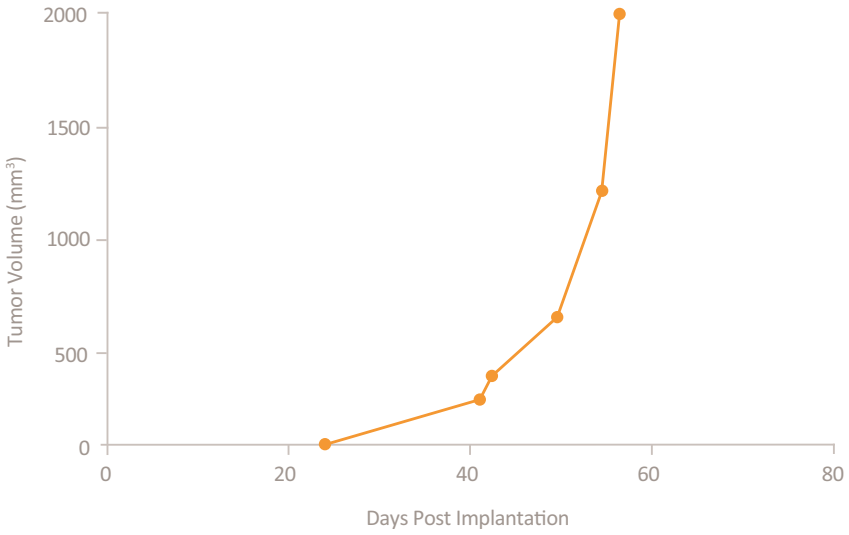

Development of a CDX Model

A CDX model was established by intravenously injecting B-NDG mice with $5x10^6$ Raji leukemia cells. BALB/c nude and NOD-scid mice were also injected with the same number of Raji cells for comparison. For all three models, body weight change (relative to the weight at inoculation) was measured weekly for 30 days post injection, and the percentage change of human cells in mouse peripheral blood was assessed using qPCR. As shown in Figure 10A, the B-NDG mice lost approximately 20% of their body weight between Days 12 and 18, while the BALB/c nude animals maintained a relatively stable weight and the NOD-scid animals initially gained weight, followed by a drop of approximately 30% between days 18 and 25.

Figure 10B shows the percent of human cells in mouse whole blood over time. While the BALB/c nude and NOD-scid models reached a maximum of approximately 10% and 30% human cells, respectively, the B-NDG model showed a maximum of between 60 and 70% human cells. Immunohistochemical staining also showed higher levels of human cells in the liver and spleen of B-NDG mice versus NOD-scid mice using a human specific antibody (Figure 10C).

Figure 10: Raji leukemia cell growth in B-NDG mice. (A) Body weight. (B) Percentage of human cells in mouse peripheral blood. (C) Immunohistochemical staining of liver and spleen of NOD-scid and B-NDG animals after Raji cell inoculation. Tissues were harvested after the weight of the mice was reduced by more than 20% after inoculation. Antibody used was an anti-human mitochondrial membrane protein antibody (Millipore, MAB1273).

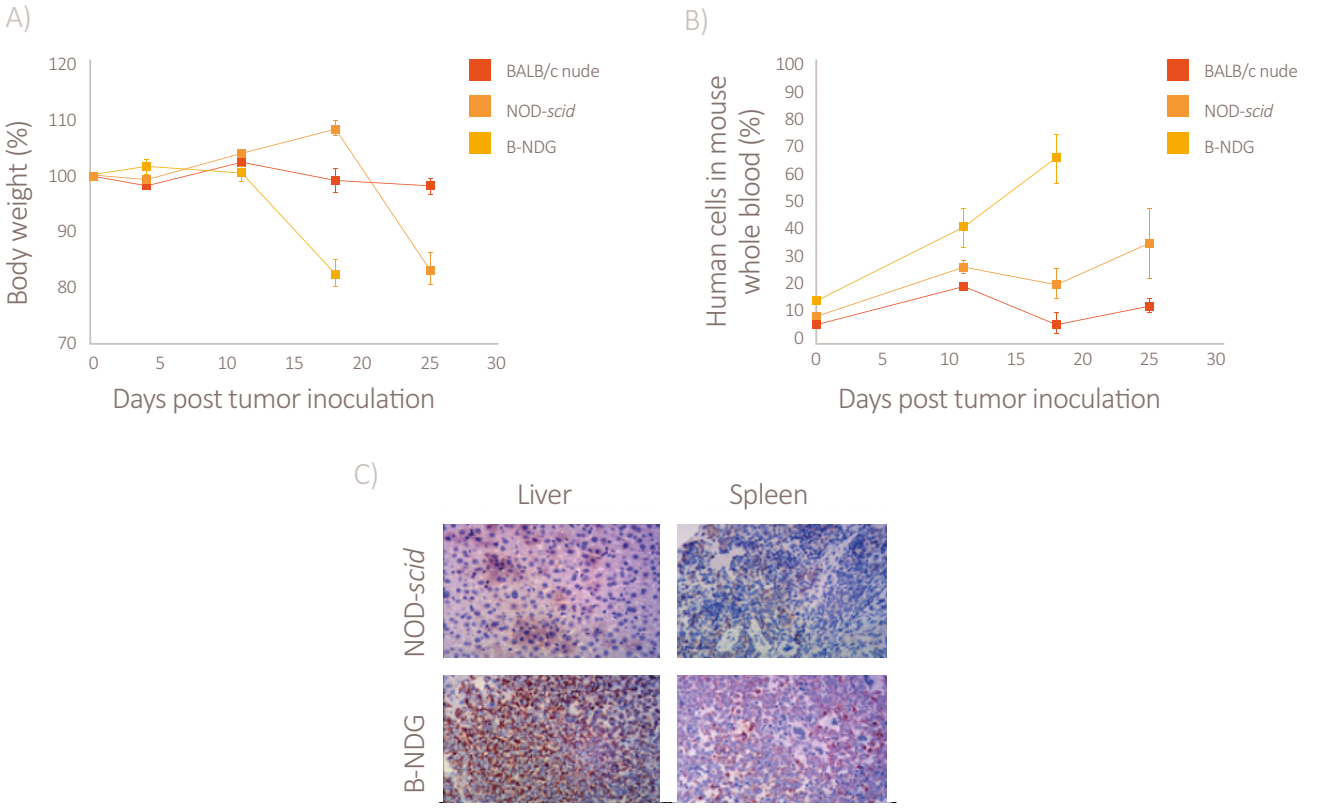

Applications of the B-NDG model

Over the past few years, the B-NDG model has been used in an increasing number of peer-reviewed publications for a variety of applications; the reference section of this paper provides a bibliography of these studies.

Below, we highlight the results from two of these publications. Chen et al. (2019a) established a colorectal cancer (CRC) PDX model with the B-NDG mouse that was successfully used for drug-sensitivity testing, and Chen *et al.* (2020a) devised a novel CAR-T-based treatment strategy.

PDX COLORECTAL MODEL FOR DRUG-SENSITIVITY TESTING

Chen et al. (2019a) sought to better understand the role of the eukaryotic initiation factor 4A2 (EIF4A2) in CRC and evaluate the *in vivo* efficacy of silvestrol and oxaliplatin (singly or in combination) against colorectal tumors. The investigators developed CRC PDX models by xenografting patient tumor samples into the flanks of B-NDG mice. Successfully established PDXs were then passaged into a second generation of B-NDG mice, which were used for the *in vivo* drug efficacy testing once the tumors had reached ~600 mm^3. The animals were injected with the respective drugs every three days for four weeks. Overall, from a mechanistic perspective, it was determined that EIF4A2 promotes experimental metastasis and oxaliplatin resistance in CRC, and silvestrol inhibited tumor growth and had a synergistic effect with oxaliplatin to induce apoptosis in PDXs (Figure 11).

Figure 11: Silvestrol (SIL) inhibits tumor growth and has synergistic effects with oxaliplatin (OXA) in PDXs. Control vehicle is phosphate buffered saline (PBS). From Chen ZH, et al. (2019a). Eukaryotic initiation factor 4A2 promotes experimental metastasis and oxaliplatin resistance in colorectal cancer.

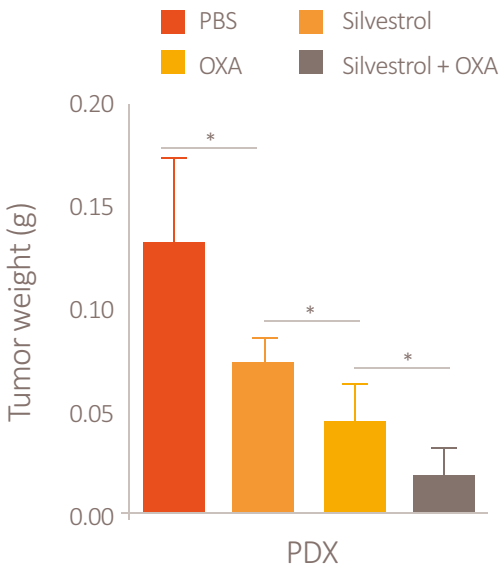

Novel Strategy for Developing Memory CAR-T Cells

Treatment with CAR-modified T cells targeting CD19 has shown amazing clinical success in patients with relapsed/refractory B cell malignancies; however, remission is not sustained in a substantial number of patients. Thus, Chen et al. (2020a) sought to emulate the concept of a vaccine immunization protocol to optimize CAR-T-19 therapy by using cells expressing tumor antigens to evaluate whether the activity of CAR-T cells could be maintained.

To establish the model, B-NDG mice received $5x10^5$ Raji-Fluc cells via tail vein injection on day 0, followed by an injection of $2x10^7$ CAR-T-19 cells between days 5 and 7 and an injection of different doses of antigen-positive Raji-Fluc, irradiated Raji-Fluc, or autologous CD19-modified T cells (expressing human CD19) between days 10 and 12.

As expected, the authors found that the CAR-T cells proliferated rapidly and killed the Raji tumor cells up until day 9, after which very few circulating tumor cells were detected and the number of CAR-T cells declined over time. Notably, the injection of a second antigen (autologous CD19-modified T cells or live Raji cells) after the elimination of Raji cancer cells resulted in the re-stimulation of CAR-T cells and maintenance of their proliferative ability, in addition to improving survival and delaying tumor occurrence. Further, the autologous CD19-modified T cells facilitated the generation of memory CAR-T cells. Overall, the survival of the animals given the sequential treatments was superior as compared to that of the animals that received the single treatment of CAR-T cells. The authors concluded that these results provide a new strategy for generating memory CAR-T cells, which may increase clinical efficacy of CAR-T therapy.

Summary: The B-NDG ultra-immunodeficient mouse harbors several features that translate into many benefits as compared to other immunodeficient models. This model has successfully been used in peer-reviewed publications to establish PDX and CDX models and is well suited for studies that require humanization, using either PBMCs or HSCs.

B-NDG model references

Ao, Xiang; Yang, Yu; Li, Weiqiang; Tan, Yan; Guo, Wei; Ao, Luoquan; He, Xiao; Wu, Xiaofeng; Xia, Jianchuan; Xu, Xiang; Guo, Jianxin;Anti-αFR CAR-engineered NK-92 Cells Display Potent Cytotoxicity Against αFR-positive Ovarian Cancer. Journal of immunotherapy (Hagerstown, Md.: 1997) Vol.42, 2019

Chen, Ruifeng; Wang, Meng; Liu, Qiang; Wu, Jiajing; Huang, Weijing; Li, Xuejiao; Du, Baohua; Xu, Qilong; Duan, Jingjing; Jiao, Shunchang; Lee, Hyun Soo; Jung, Nam-Chul; Lee, Jun-Ho; Wang, Yu; Wang, Youchun; Sequential treatment with aT19 cells generates memory CAR-T cells and prolongs the lifespan of Raji-B-NDG mice. Cancer letters Vol.469, 2020a

Chen, Hua-Dong; Huang, Chen-Song; Xu, Qiong-Cong; Li, Fuxi; Huang, Xi-Tai; Wang, Jie-Qin; Li, Shi-Jin; Zhao, Wei; Yin, Xiao-Yu; Therapeutic Targeting of CDK7 Suppresses Tumor Progression in Intrahepatic Cholangiocarcinoma. International journal of biological sciences Vol.16, 2020b

Chen, Zhan-Hong; Qi, Jing-Jing; Wu, Qi-Nian; Lu, Jia-Huan; Liu, Ze-Xian; Wang, Yun; Hu, Pei-Shan; Li, Ting; Lin, Jin-Fei; Wu, Xiang-Yuan; Miao, Lei; Zeng, Zhao-Lei; Xie, Dan; Ju, Huai-Qiang; Xu, Rui-Hua; Wang, Feng; Eukaryotic initiation factor 4A2 promotes experimental metastasis and oxaliplatin resistance in colorectal cancer. Journal of experimental & clinical cancer research: CR Vol.38, 2019a

Chen, Wancheng; Wang, Xuefei; Zhao, Bingxia; Zhang, Rongjun; Xie, Zhen; He, Yi; Chen, Ali; Xie, Xiaofang; Yao, Kaitai; Zhong, Mei; Yuan, Miaomiao; CuS-MnS2 nano-flowers for magnetic resonance imaging guided photothermal/photodynamic therapy of ovarian cancer through necroptosis. Nanoscale Vol.11, 2019b

Chen, Zhicong; He, Shiming; Zhan, Yonghao; He, Anbang; Fang, Dong; Gong, Yanqing; Li, Xuesong; Zhou, Liqun; TGF-β-induced transgelin promotes bladder cancer metastasis by regulating epithelial-mesenchymal transition and invadopodia formation. EBioMedicine Vol.47, 2019c

Dai, Kai; Huang, Yabing; Chen, Zubing; Sun, Xiaomei; Yang, Lihua; Jiang, Yingan; Kbtbd2 inhibits the cytotoxic activity of immortalized NK cells through down-regulating mTOR signaling in a mouse hepatocellular carcinoma model. European journal of immunology Vol.48, 2018

Gao, Xiaomei; Dai, Charles; Huang, Shengsong; Tang, Jingjie; Chen, Guoyuan; Li, Jianneng; Zhu, Ziqi; Zhu, Xuyou; Zhou, Shuirong; Gao, Yuanyuan; Hou, Zemin; Fang, Zijun; Xu, Chengdang; Wang, Jianyang; Wu, Denglong; Sharifi, Nima; Li, Zhenfei; Functional Silencing of HSD17B2 in Prostate Cancer Promotes Disease Progression. Clinical cancer research: an official journal of the American Association for Cancer Research Vol.25, 2019

Gong, Jianhua; Guo, Feihu; Cheng, Weihua; Fan, Hongqiang; Miao, Qingfang; Yang, Jigang; Preliminary biological evaluation of 123I-labelled anti-CD30-LDM in CD30-positive lymphomas murine models. Artificial cells, nanomedicine, and biotechnology Vol.48, 2020

Guo, Rongqun; Hu, Fangxiao; Weng, Qitong; Lv, Cui; Wu, Hongling; Liu, Lijuan; Li, Zongcheng; Zeng, Yang; Bai, Zhijie; Zhang, Mengyun; Liu, Yuting; Liu, Xiaofei; Xia, Chengxiang; Wang, Tongjie; Zhou, Peiqing; Wang, Kaitao; Dong, Yong; Luo, Yuxuan; Zhang, Xiangzhong; Guan, Yuxian; Geng, Yang; Du, Juan; Li, Yangqiu; Lan, Yu; Chen, Jiekai; Liu, Bing; Wang, Jinyong; Guiding T lymphopoiesis from pluripotent stem cells by defined transcription factors. Cell research Vol.30, 2020

Huang, Weimei; Yang, Yunchu; Wu, Jingfang; Niu, Yuchun; Yao, Yao; Zhang, Jian; Huang, Xiaoxian; Liang, Shumei; Chen, Rui; Chen, Size; Guo, Linlang; Circular RNA cESRP1 sensitises small cell lung cancer cells to chemotherapy by sponging miR-93-5p to inhibit TGF-β signalling. Cell death and differentiation Vol.27, 2020

Lei, Hu; Tu, Yaoyao; Yang, Li; Jin, Jin; Luo, Hao; Xu, Hanzhang; Kang, Jingwu; Zhou, Li; Wu, Yingli; Quinacrine Depletes BCR-ABL and Suppresses Ph-Positive Leukemia Cells. Cancer investigation Vol.37, 2019

Lin Q., Lee M., Guo Y., Gan T. The human immune system reconstituted B-NDG mouse models are ideal tools for CAR-T and therapeutic antibody preclinical efficacy evaluation [abstract]. In: Proceedings of the American Association for Cancer Research Annual Meeting 2019; 2019 Mar 29-Apr 3; Atlanta, GA. Philadelphia (PA): AACR; Cancer Res 2019;79(13 Suppl):Abstract nr 1052.

Li, Yifan; Gong, Yanqing; Ning, Xianghui; Peng, Ding; Liu, Libo; He, Shiming; Gong, Kan; Zhang, Cuijian; Li, Xuesong; Zhou, Liqun; Downregulation of CLDN7 due to promoter hypermethylation is associated with human clear cell renal cell carcinoma progression and poor prognosis. Journal of experimental & clinical cancer research: CR Vol.37, 2018

Sun, Bin; Yang, Dong; Dai, Hongjiu; Liu, Xiuyun; Jia, Ru; Cui, Xiaoyue; Li, Wenxuan; Cai, Changchun; Xu, Jianming; Zhao, Xudong; Eradication of Hepatocellular Carcinoma by NKG2D-Based CAR-T Cells. Cancer immunology research Vol.7, 2019

Sun, Yu; Sun, Ye; Yan, Kun; Li, Zhuxuan; Xu, Cheng; Geng, Yibo; Pan, Changcun; Chen, Xin; Zhang, Liwei; Xi, Qiaoran; Potent anti-tumor efficacy of palbociclib in treatment-naïve H3.3K27M-mutant diffuse intrinsic pontine glioma. EBioMedicine Vol.43, 2019

Wang, Dan; Chen, Yao; Fang, Houshun; Zheng, Liang; Li, Ying; Yang, Fan; Xu, Yan; Du, Lijuan; Zhou, Bin-Bing S; Li, Hui; Increase of PRPP enhances chemosensitivity of PRPS1 mutant acute lymphoblastic leukemia cells to 5-Fluorouracil. Journal of cellular and molecular medicine Vol.22, 2018

Wang, Jingbo; Shao, Lijuan; Wu, Liujing; Ma, Wei; Zheng, Yuanyuan; Hu, Chaofeng; Li, Furong; Expression levels of a gene signature in hiPSC associated with lung adenocarcinoma stem cells and its capability in eliciting specific antitumor immune-response in a humanized mice model. Thoracic cancer Vol.7, 2020

Wang, Qiongyao; Zeng, Fanrui; Sun, Yanqin; Qiu, Qianqian; Zhang, Jian; Huang, Weimei; Huang, Jie; Huang, Xiaomin; Guo, Linlang; Etk Interaction with PFKFB4 Modulates Chemoresistance of Small-cell Lung Cancer by Regulating Autophagy. Clinical cancer research: an official journal of the American Association for Cancer Research Vol.24, 2018

Wu, Rihui; Mei, Xueting; Ye, Yibiao; Xue, Ting; Wang, Jiasheng; Sun, Wenjia; Lin, Caixia; Xue, Ruoxue; Zhang, Jiabao; Xu, Donghui; Zn(II)-curcumin solid dispersion impairs hepatocellular carcinoma growth and enhances chemotherapy by modulating gut microbiota-mediated zinc homeostasis. Pharmacological research Vol.150, 2019

Xia, Jiliang; He, Yanjuan; Meng, Bin; Chen, Shilian; Zhang, Jingyu; Wu, Xuan; Zhu, Yinghong; Shen, Yi; Feng, Xiangling; Guan, Yongjun; Kuang, Chunmei; Guo, Jiaojiao; Lei, Qian; Wu, Yangbowen; An, Gang; Li, Guancheng; Qiu, Lugui; Zhan, Fenghuang; Zhou, Wen; NEK2 induces autophagy-mediated bortezomib resistance by stabilizing Beclin-1 in multiple myeloma. Molecular oncology Vol.14, 2020

Xiao, Haowen; Ding, Yingying; Gao, Yang; Wang, Li-Mengmeng; Wang, Huafang; Ding, Lijuan; Li, Xiaoqing; Yu, Xiaohong; Huang, He; Haploinsufficiency of NR3C1 drives glucocorticoid resistance in adult acute lymphoblastic leukemia cells by down-regulating the mitochondrial apoptosis axis, and is sensitive to Bcl-2 blockage. Cancer cell international Vol.19, 2019

Xiao, Xinhua; Li, Huiliang; Jin, Huizi; Jin, Jin; Yu, Miao; Ma, Chunmin; Tong, Yin; Zhou, Li; Lei, Hu; Xu, Hanzhang; Zhang, Weidong; Liu, Wei; Wu, Yingli; Identification of 11(13)-dehydroivaxillin as a potent therapeutic agent against non-Hodgkins lymphoma. Cell death & disease Vol.8, 2017

Yang, Dong; Sun, Bin; Dai, Hongjiu; Li, Wenxuan; Shi, Lan; Zhang, Peixian; Li, Shirong; Zhao, Xudong; T cells expressing NKG2D chimeric antigen receptors efficiently eliminate glioblastoma and cancer stem cells. Journal for immunotherapy of cancer Vol.7, 2019

Zhan, Yonghao; Chen, Zhicong; He, Shiming; Gong, Yanqing; He, Anbang; Li, Yifan; Zhang, Lianghao; Zhang, Xuepei; Fang, Dong; Li, Xuesong; Zhou, Liqun; Long non-coding RNA SOX2OT promotes the stemness phenotype of bladder cancer cells by modulating SOX2. Molecular cancer Vol.19, 2020

Zhang, Panpan; Li, Xiaomin; He, Qiuping; Zhang, Lulu; Song, Keqing; Yang, Xiaojing; He, Qingmei; Wang, Yaqin; Hong, Xiaohong; Ma, Jun; Liu, Na; TRIM21-SERPINB5 aids GMPS repression to protect nasopharyngeal carcinoma cells from radiation-induced apoptosis. Journal of biomedical science Vol.27, 2020

Zhao, Bixing; Wang, Yingchao; Tan, Xionghong; Zheng, Xiaoyuan; Wang, Fei; Ke, Kun; Zhang, Cuilin; Liao, Naishun; Dang, Yuan; Shi, Yingjun; Zheng, Youshi; Gao, Yunzhen; Li, Qin; Liu, Xiaolong; Liu, Jingfeng; An Optogenetic Controllable T Cell System for Hepatocellular Carcinoma Immunotherapy. Theranostics Vol.9, 2019

inōtiv

analyze. answer. advance.

For more information, please visit
inotivco.com/oncology